BAMS Article

# Climate Change Contributions to Increasing Compound Flooding Risk in New York City

Ali Sarhadi, Raphaël Rousseau-Rizzi, Kyle Mandli, Jeffrey Neal, Michael P. Wiper, Monika Feldmann, and Kerry Emanuel

**KEYWORDS:**
Climate change; Tropical cyclones; Extratropical cyclones

**ABSTRACT:** Efforts to meaningfully quantify the changes in coastal compound surge- and rainfall-driven flooding hazard associated with tropical cyclones (TCs) and extratropical cyclones (ETCs) in a warming climate have increased in recent years. Despite substantial progress, however, obtaining actionable details such as the spatially and temporally varying distribution and proximal causes of changing flooding hazard in cities remains a persistent challenge. Here, for the first time, physics-based hydrodynamic flood models driven by rainfall and storm surge simultaneously are used to estimate the magnitude and frequency of compound flooding events. We apply this to the particular case of New York City. We find that sea level rise (SLR) alone will increase the TC and ETC compound flooding hazard more significantly than changes in storm climatology as the climate warms. We also project that the probability of destructive Sandy-like compound flooding will increase by up to 5 times by the end of the century. Our results have strong implications for climate change adaptation in coastal communities.

https://doi.org/10.1175/BAMS-D-23-0177.1
Corresponding author: Ali Sarhadi, sarhadi@mit.edu
Supplemental material: https://doi.org/10.1175/BAMS-D-23-0177.2
In final form 15 October 2023

**AFFILIATIONS: Sarhadi, Rousseau-Rizzi, and Emanuel**—Lorenz Center, Department of Earth Atmospheric and Planetary Sciences, Massachusetts Institute of Technology, Cambridge, Massachusetts; **Mandli**—Department of Applied Physics and Applied Mathematics, Columbia University, New York, New York; **Neal**—School of Geographical Sciences, University of Bristol, Bristol, United Kingdom; **Wiper**—Department of Statistics, Universidad Carlos III de Madrid, Madrid, Spain; **Feldmann**—Environmental Remote Sensing Laboratory, École Polytechnique Fédérale de Lausanne, Lausanne, and Radar, Satellite and Nowcasting Division, MeteoSwiss, Locarno, Switzerland

Tropical cyclones (TCs) and extratropical cyclones (ETCs) are among the deadliest and most destructive natural hazards, causing substantial fatalities and economic damages [$26 billion from TCs and $2 billion (U.S. dollars) from winter ETCs each year in the United States alone] (Bakkensen and Mendelsohn 2019; Smith et al. 2020). Among multiple hazards associated with these cyclones, many of the fatalities and much of the damage are caused by coastal flooding from storm surge (generated by high-speed winds), and inland flooding rain driven in coastal and inland communities (Zhang et al. 2018; Rappaport 2014). During destructive cyclones, each of these flooding hazards may play a role, either separately or in combination. For example, strong winds during Hurricane Sandy in October 2012 caused devastating surge-driven flooding across heavily populated coastal areas in New York City (NYC), resulting in more than $64 billion (2017 U.S. dollars) in damages (Strauss et al. 2021). Hurricane Harvey in August 2017, instead, stalled over an inland area and poured an unprecedented heavy rainfall for many days over the Houston metropolitan area, causing catastrophic inland flooding and costing $125 billion (2017 U.S. dollars) in damages (Zhang et al. 2018). However, storm surge-driven flooding may co-occur with inland heavy rainfall-driven flooding resulting in a compound flooding event, whose destructive potential is often much greater than that of either of the individual flooding components. During the landfall of Hurricane Katrina, a destructive category 3 TC, a significant storm surge coincided with record-breaking heavy inland rainfall along the Gulf Coast. The compound flooding devastated coastal areas in Louisiana and caused one of the costliest natural disasters in U.S. history, with at least 1,833 deaths (Waters 2016) and more than $160 billion in damages (adjusted to 2017 U.S. dollars to compare with the rainfall dominant Hurricane Harvey) (Patricola and Wehner 2018). Recently, a destructive compound flooding event during Hurricane Ian had devastating impact in western Florida and cost $67 billion in insured losses (Palm and Bolsen 2023). In densely populated coastal areas, such compound flooding in TCs or ETCs can thus lead to extreme impacts even if, individually, these flooding hazards are not extreme (Wahl et al. 2015).

Past and future changes in the probability of compound flooding from these cyclones depend on how the warming atmosphere and oceans have influenced and will influence the structural characteristics, intensity, frequency, and movement of these cyclones (Emanuel 2021b). There is confidence that anthropogenic warming has intensified the activity and destructiveness of major TCs in the North Atlantic basin in recent decades (Bender et al. 2010; Emanuel 2005, 2021a, 2013). This trend is expected to accelerate in the future as ocean temperatures increase (Trenberth et al. 2018; Saunders and Lea 2008; Emanuel 2005; Huang et al. 2015), and the troposphere warms (Patricola and Wehner 2018; Emanuel 2021b; Walsh et al. 2015; Priestley and Catto 2022). Despite our understanding of the future changes

of multiple individual drivers of TC and ETC flooding under a warming climate—including intensifying rainfall, poleward migration, slowdown of cyclone translation speed, sea level rise (SLR), and deceleration of ETCs due to atmospheric blocking (Emanuel 2021b; Kossin et al. 2014; Booth et al. 2021; Strauss et al. 2021)—quantifying the probability of compound flooding in response to these changes in highly populated coastal cities, like NYC, remains elusive.

In recent years, significant attention has been directed toward modeling the complex hydrodynamics of compound flooding in coastal areas. Statistical methodologies are commonly employed to assess the probability of flooding by developing joint statistical distributions that capture the dependence between the individual contributions to the flooding (Gori et al. 2022; Gori and Lin 2022; Wahl et al. 2015; Moftakhari et al. 2017). However, this approach has limitations that introduce uncertainty in hazard estimation. First, it overlooks the physical spatiotemporal interactions between surge- and rainfall-driven flooding, relying on statistical dependence measures to address the interaction. Moreover, it neglects hydraulic compound flooding, which involves converting surge height and rainfall intensity into flooding levels, while simultaneously accounting for the compound effect of these individual components. Instead, the prevalent practice is to treat rainfall intensity and surge height as separate hazards and combine them using joint distributions, resulting in uncertain evaluations of compound flooding probability.

In recent years, there have been advancements in the integration of physically based computational models to enhance statistical hazard assessment methodologies (Garner et al. 2017; Reed et al. 2015; Lin et al. 2016; Marsooli et al. 2019; Roberts et al. 2017; Lin et al. 2019). Nevertheless, the predominant emphasis has been on examining individual contributions, particularly surge inundation flooding. These models often disregard the pivotal influence of rainfall in compound flooding dynamics and overlook the hydraulic mechanisms responsible for transforming surge height into subsequent flood levels. Furthermore, certain models solely concentrate on evaluating the hazard associated with rainfall in cyclonic events (Emanuel 2017; Bates et al. 2021; Xi and Lin 2022a,b), highlighting the necessity for a holistic framework that encompasses the synergistic impacts of both rainfall and surge in compound flooding occurrences.

In this study, we introduce an innovative approach to address the limitations of previous methodologies for simulating compound flooding dynamics. Our method utilizes a physically based numerical hydrodynamic model to simultaneously simulate compound flooding by converting individual drivers into hydraulic-based flood simulations. Compound flooding arises from the complex interaction between storm surge- and heavy rainfall-driven flooding. Our study explicitly models this intricate hydrodynamic interplay between the two sources of water with high temporal and spatial resolution.

To do so, first, we estimate the climatology and evolution of TCs in the current and future climates by using a physics-based statistical–deterministic downscaling approach (Emanuel et al. 2008). This method generates a large number of synthetic TCs consistent with the ERA-Interim and general circulation model (GCM) climates to emulate a long record of historical and future TC events. We downscale a large set of storms from ERA-Interim from the late-twentieth-century (1979–99) and the early-twenty-first century (2000–20) climates. We also downscale a large set of synthetic tracks from four bias corrected GCMs of the Coupled Model Intercomparison Project phase 6 (CMIP6), to represent the evolution of TCs in the current climate (2000–14), and at the middle (2041–60) and end of the century (2081–2100) under the SSP3–7.0 scenario. The Tropical Cyclone Rainfall (TCR) algorithm is used to estimate evolving, high-spatial-resolution (almost ~20 m) hourly rainfall from the synthetic TCs in and near NYC (Feldmann et al. 2019). Second, for ETC events, we use a dynamically downscaled dataset of hourly rainfall, wind, and

pressure fields over the northeastern United States, with 3-km spatial resolution, driven by CESM v1.0 under representative concentration pathway 8.5 (RCP8.5). The downscaling data come from convection-permitting Weather Research and Forecasting (WRF) Model simulations for almost the same three climate periods (Komurcu et al. 2018). We then use an extensively evaluated hydrodynamic model (GeoClaw) driven by atmospheric pressure and surface wind speed to compute surge height associated with TCs and ETCs, along a vast segment of coastline near NYC (Mandli and Dawson 2014). The hydrodynamic model also accounts for SLR from the ensemble mean of CMIP6 projections, incorporated to the model as a "bathtub" approach (see more details on the datasets in the appendix).

We then introduce a novel compound pluvial flood modeling framework that combines high-spatiotemporal-resolution surge height, simulated using a version of GeoClaw (Mandli and Dawson 2014) that we modified, with hourly cyclone rainfall intensity. This framework extends the capabilities of the existing LISFLOOD-FP hydraulic model (Neal et al. 2012), by incorporating these two components as simultaneous boundary conditions. Consequently, it enables the simulation of intricate hydrodynamic interactions between surge- and rainfall-driven flooding in coastal regions. The primary objective is to enhance understanding of compound flooding events, particularly those resulting from cyclones in coastal cities. Additionally, we investigate the potential impacts of SLR and changes in the climatology of TCs and ETCs on future flooding hazards in NYC. Figure 1 presents a flowchart outlining step-by-step procedures to achieve our stated objectives. Further details can be found in the appendix. Our research aims to advance scientific knowledge in this field, improve hazard assessment and management strategies, and contribute to coastal planning and adaptation efforts.

## Compound flooding effect

Figures 2a–d compare the behavior of compound flooding with the individual surge- and rainfall-driven flooding in different locations in NYC (coastal and inland areas), based on the simulations from a randomly selected synthetic TC track in the current climate in NYC. Figure 2a depicts the maximum flood levels spatially during the landfall of the synthetic TC. It should be noted that the elevated flood levels along the Passaic River in New Jersey result from the response of small catchment areas with a very low percentage of impervious surfaces to heavy rainfall, as well as the backwater effect caused by surge-driven flooding (Levinson 2018; Saleh et al. 2017). In coastal areas, as illustrated in Figs. 2b–d, during the storm's landfall, storm surge– and rainfall-driven flooding dynamically interact across both temporal and spatial dimensions. This intricate interplay reveals that their combined effects are not simply linearly additive. Instead, they exhibit a synergistic relationship, mutually reinforcing each other, and resulting in compound flooding characterized by heightened magnitude and expanded spatial coverage of coastal inundation. This complex and nonlinear effect depends on different factors, including the nature of the storm (whether it is wind or rainfall dominant), topography, and the distance from coastline, and the lag time between surge- and rainfall driven flooding. Although the contribution of surge-driven flooding dominates in coastal areas, in inland areas rainfall-driven flooding is the dominant factor. In both coastal and inland areas, however, the compound flooding levels are higher than the individual contributions at the time of landfall. We also show that a linear summation of the individual surge- and rainfall-driven flooding (red dashed line) cannot represent the level of compound flooding. Summing the two individual flooding levels overestimates the level of "actual" compound flooding.

This effect of compounding will also affect hazard assessments in the current and future warming climate. In assessing TC flood hazard, different studies typically consider one

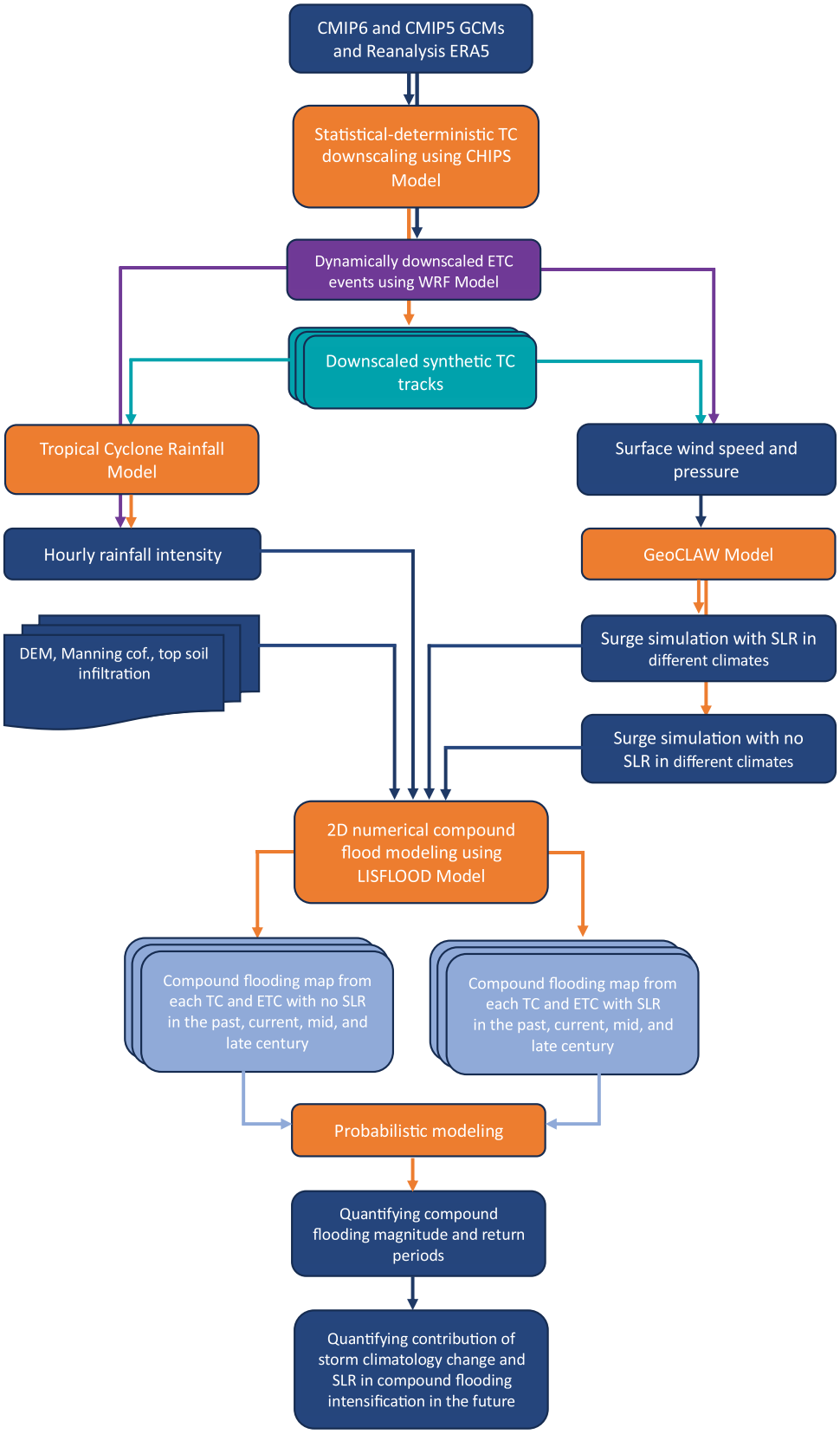


**Fig. 1. Flowchart illustrating the methodology developed for compound flood modeling of tropical and extratropical cyclones and their associated hazards under a changing climate.**

individual contribution (Lin et al. 2016, 2012; Reed et al. 2015) and use statistical algorithms to account for other components (Bates et al. 2021; Gori et al. 2022). These approaches, however, ignore the spatiotemporal nonlinear mechanical interactions between the surge- and

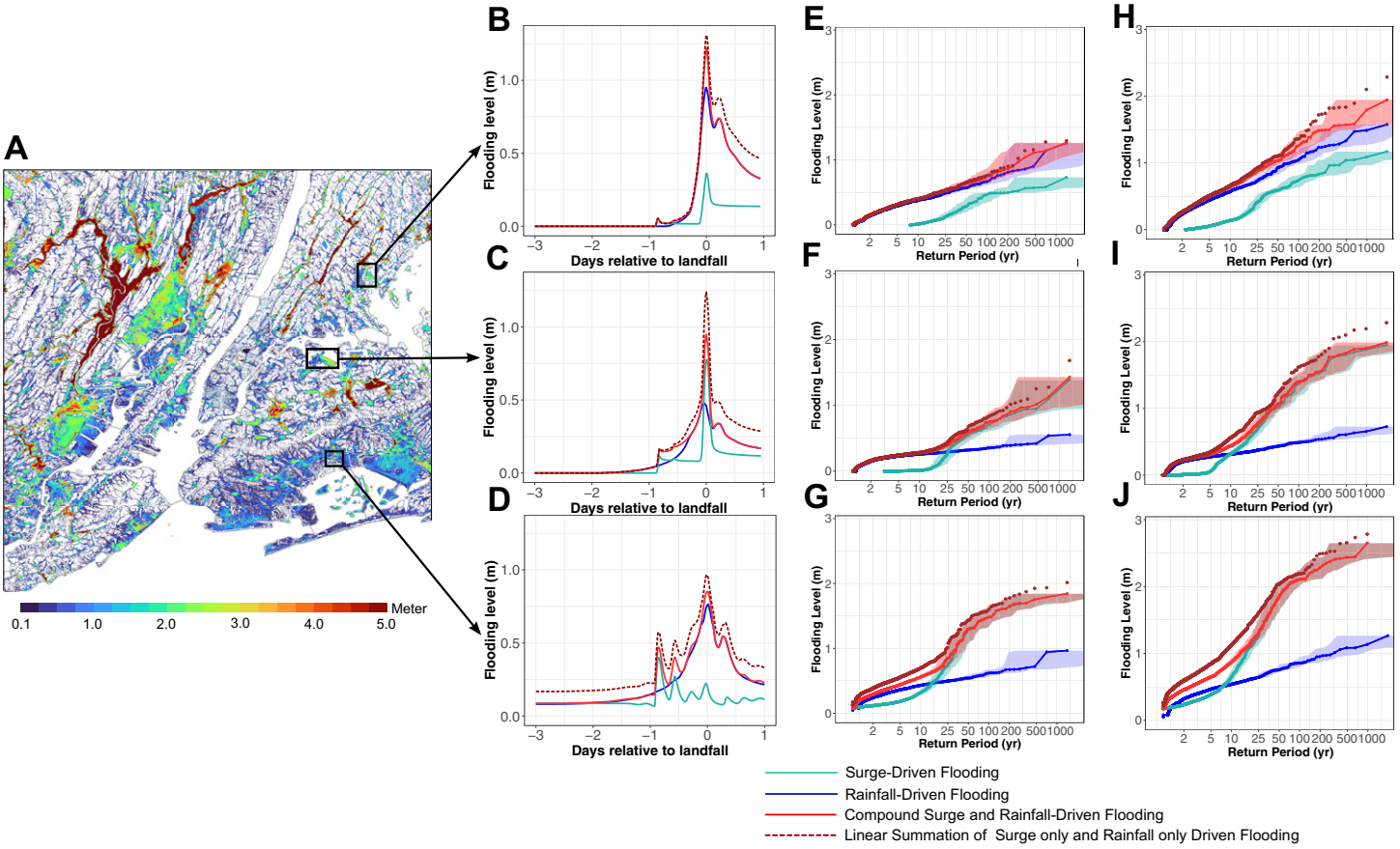


**Fig. 2. (a) Maximum compound flooding level for a downscaled synthetic track (#260) from CESM2 model under the current climate. (b)–(d) Compounding effect from nonlinear mechanical interaction between surge- and rainfall-driven flooding through landfalling the synthetic TC in the three depicted areas in NYC. (e)–(g) Flooding levels as a function of return period from the three flooding hazard sources. The results are based on synthetic TCs generated from CESM2 model over the current climate (the results are calculated based on the mean of flooding levels for each depicted area). The shading in the figure represents sampling uncertainty bounds calculated based on the 5th and 95th percentiles of a Poisson distribution. (h)–(j) As in (e)–(g), but for the end of the century. Water levels are referenced to the vertical datum of NAVD88.**

rainfall-driven flooding, which can lead to higher potential for compound flooding across the coastal and inland areas. For example, Fig. 2e shows that relying on only surge-driven flooding in inland areas underestimates the magnitude of actual compound flooding up to 56.3% (51.0%–61.6%) in the current climate, and up to 56.15% (55.8%–56.5%) in the late twenty-first century for the events which occur once in 100 years (Fig. 2h). In coastal areas, however, relying on only rainfall-driven flooding underestimates the magnitude of compound flooding by up to 40.0% (41.8%–42.2%) in the current climate, and by up to 40.5% (39.3%–41.7%) in the late twenty-first century for the same events (Figs. 2g,j). On the other hand, the linear summation of the individual surge- and rainfall-driven flooding overestimates the magnitude of flooding compared to the actual compound flooding. This misestimation of the hazard is more serious for the low-frequency events in the upper tail in both current and future climates. Therefore, it is crucial to account for the dynamic spatiotemporal, nonlinear compound effects of surge- and rainfall-driven flooding during landfall, as well as their impacts on coastal and inland areas, in order to comprehensively assess the risk of coastal flooding.

In addition to examining complex and nonlinear compound flooding, we provide an illustrative example in Fig. S1 in the online supplemental material (https://doi.org/10.1175/BAMS-D-23-0177.2) to compare the effects of key drivers, specifically rainfall intensity and surface wind speed, on the magnitude of compound flooding.

## Hurricane Sandy's flooding

To reconstruct the flooding caused by Hurricane Sandy in 2012 in NYC, we evaluated surge height simulations from GeoClaw by comparing them with actual recorded surge data obtained from the National Oceanic and Atmospheric Administration (NOAA) and the best track dataset. Additionally, we simulated surge height from a synthetic TC event closely resembling Hurricane Sandy, at the Battery gauge in Lower Manhattan, as depicted in Figs. 3a and 3b. Compared to the NOAA observations (blue), GeoClaw accurately simulates surge heights, achieving an accuracy of more than 82%, for both the Sandy-like hurricane (red) and the best track data (green). Furthermore, in Fig. 3c, we compared the simulated surge-driven flooding extent from the Sandy-like hurricane (red) to the observed FEMA flood inundation map (blue), which serves as the sole available evidence for evaluation. The results exhibit a high level of accuracy, exceeding 80%.

It is important to acknowledge the complexities associated with simulating a storm as multifaceted as Hurricane Sandy, which transitioned from a tropical cyclone to an extratropical cyclone near the time of landfall. Given the unique characteristics of Sandy, it is challenging to replicate all exact parameters of the storm. Therefore, we considered

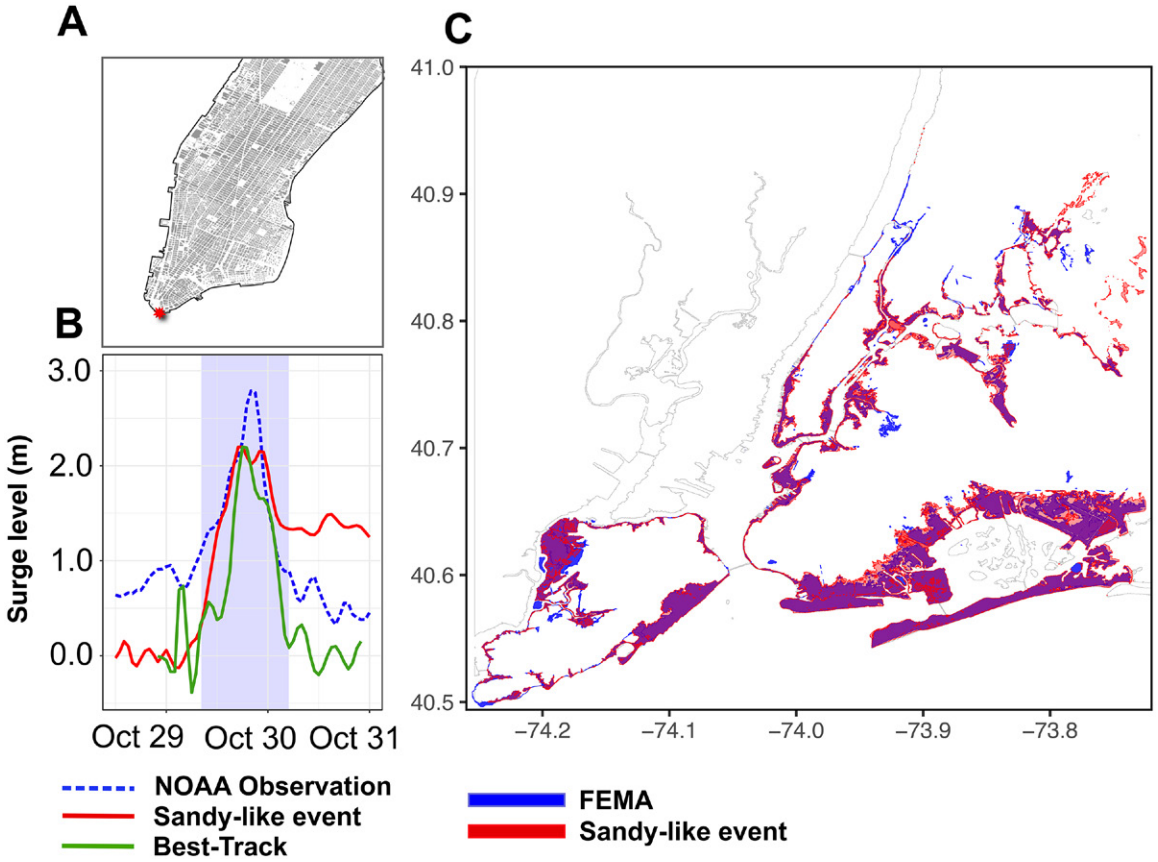


**Fig. 3. Performance evaluation of the GeoClaw model and LISFLOOD-FP hydraulic model in simulating surge height and surge-driven flooding caused by Hurricane Sandy in October 2012 in NYC. (a) Location of the Battery gauge in Lower Manhattan. (b) Actual surge height (m) (detided NOAA water level) recorded at the Battery gauge (blue line), and simulated surge height using GeoClaw at the same location based on actual surface wind of 70 kt and central pressure of 945 hPa at the time of landfall (Blake et al. 2013) from best track data (green line), along with the simulated surge based on the Sandy-like hurricane with almost identical features (red line). (c) Flood extent map during Hurricane Sandy obtained from FEMA observations in NYC (blue), and simulated flooding extent map from the Sandy-like event (synthetic track #1299 downscaled from ERA-Interim) (red) using LISFLOOD-FP model, limited to NYC. (Note that the FEMA map depicts inundated areas, not flood levels. The simulated map is provided for comparison purpose in the same way.) The FEMA flood inundation map can be downloaded from https://data.cityofnewyork.us/Environment/Sandy-Inundation-Zone/uyj8-7rv5.**

the potential manifestation of compound flooding resulting from the selected Sandy-like event, which adequately captures the primary aspects of the storm, particularly the surge component, while acknowledging certain limitations in simulating the rainfall component. Figure 4 summarizes this particular event, showing the maximum wind speed ~70 kt (1 kt ≈ 0.51 m $s^{-1}$) experienced at landfall (Fig. 4a), and the accumulated hourly rainfall from this event (Fig. 4b). Figures 4c and 4d show, respectively, the maximum surge-driven flooding, and rainfall-driven flooding from this event. Figure 4e illustrates the potential compound flooding resulting from both storm surge and rainfall during the Sandy-like event. It is noteworthy that while storm surge played a dominant role in causing the flooding in Hurricane Sandy, rainfall also contributed to the flooding in some coastal areas (Blake et al. 2013). Figures 4c–e show that the individual rainfall and surge hazards, as well as the compound hazard, may affect different areas. Figure 4f also shows underestimation of the property value exposure under different levels of flooding from the individual hazards compared to the exposure from compound flooding during the Sandy-like event. It is clear that accounting only for individual flooding hazards misestimates the magnitude, damage, and spatial consequences relative to compound flooding. In addition, the spatial information provided by our physics-based model, which identified the most hazardous zones, is crucial for adaptation measures and cannot be well simulated using statistical methods alone.

## Tropical cyclone compound flooding risk in today's climate

Next, we quantify the extent to which anthropogenic warming has already changed the risk of compound flooding via changes in TC climatology and SLR in and near NYC. To do so, we simulate the maximum compound flooding level from 1,250 synthetic TCs downscaled from ERA-Interim under the late-twentieth-century climate, and another 1,250 events in the climate of the early twenty-first century. Figure 5a shows the changes in the return period of compound flooding between the late twentieth century and the early twenty-first century. The return period is calculated as the inverse of the annual exceedance probability defined over each of the two time periods. The results show that anthropogenic warming already has increased the magnitude of compound flooding for events with return periods between 2 and 20 years in today's climate. Sampling uncertainty, however, prevents us from distinguishing trends at larger return periods in the selected coastal area.

Figure 5b shows the spatially varying distribution of compound flooding by 100-yr return-period events for the entire study area. The results show that climate change has increased the flood levels of such events particularly in inland areas by up to ~0.5 m, caused mostly by more intense rainfall. However, there is a decreasing trend along the coastlines up to ~−0.2 m. This decrease is attributed to a decrease in the frequency of intense TCs and alterations in their tracks within the region. These changes in TC characteristics, particularly in wind speed, resulted in a decrease in surge height and subsequent compound flooding along the coastlines during recent climatic conditions. A comparison of Fig. 5 to Fig. S2, which neglects SLR, also confirms that SLR does not appear to have contributed significantly to the change in compound flooding risk in recent years. The compound flooding results for events with return periods of 25–500 years are provided in Fig. S3. The magnitude of compound flooding, especially for the low-frequency events, follows a pattern similar to that of the 100-yr return period shown in Fig. 5b, and the changes are not statistically significant in coastal areas.

## Future risk of tropical cyclone–induced compound flooding

By simulating compound flooding levels from a large set of synthetic TCs downscaled from the four climate models (i.e., CESM2, CNRM6, EC-EARTH6, and UKMO6) for the current and future climates, we quantify how the probability of compound flooding may evolve.

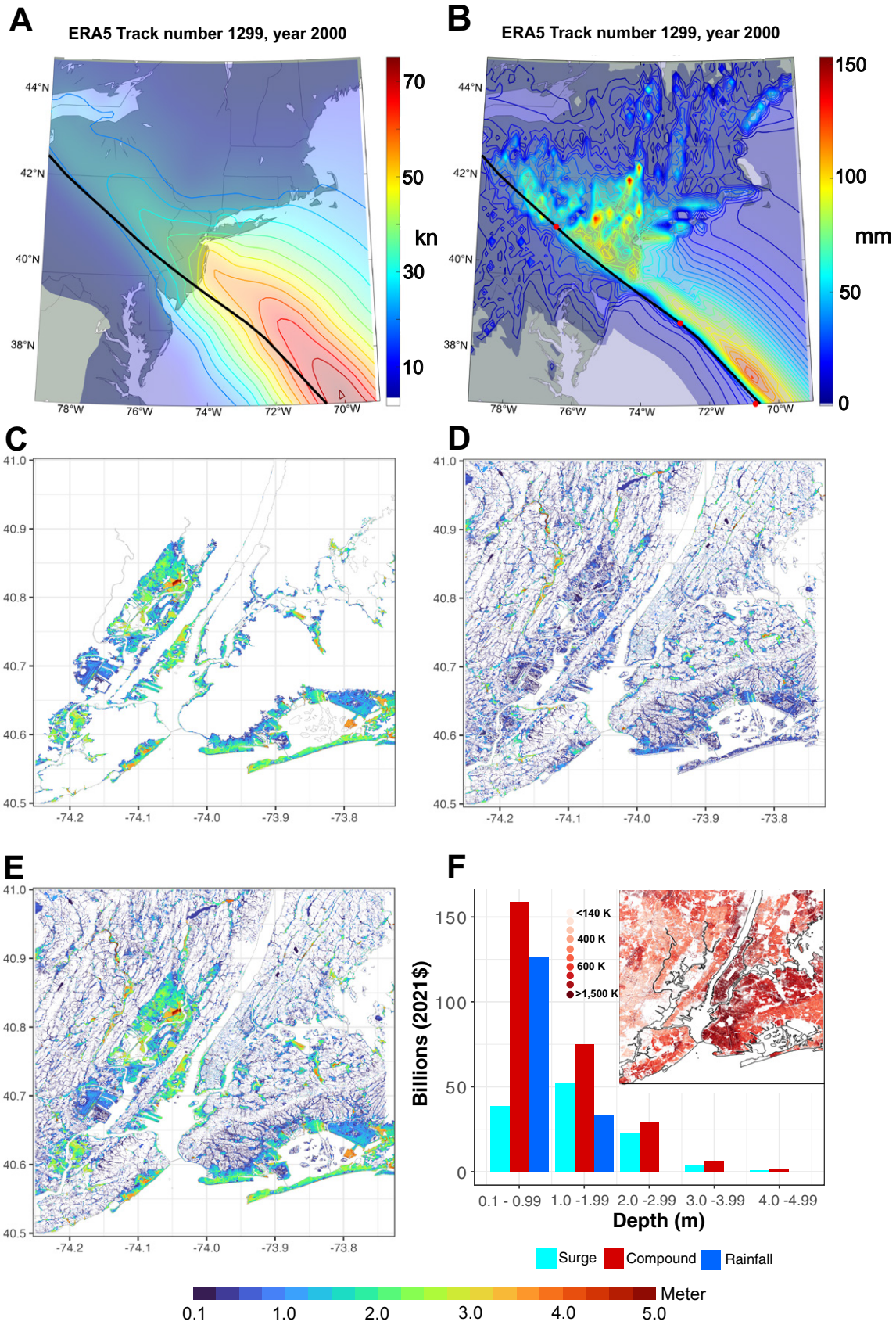


**Fig. 4. (a) Maximum wind speed swath of a Sandy-like synthetic track (#1299) downscaled from ERA5. (b) As in (a), but for rainfall accumulation. (c) Surge-driven flooding for the Sandy-like event, (d) rainfall driven flooding for the Sandy-like event, and (e) compound surge- and rainfall-driven flooding for the Sandy-like event. Water levels are referenced to the vertical datum of NAVD88. (f) Property value exposure to different levels of flooding from each flooding hazard during Hurricane Sandy in NYC (the inner map displays the values of exposed buildings, specifically, the first story, normalized to 2021 U.S. dollars).**

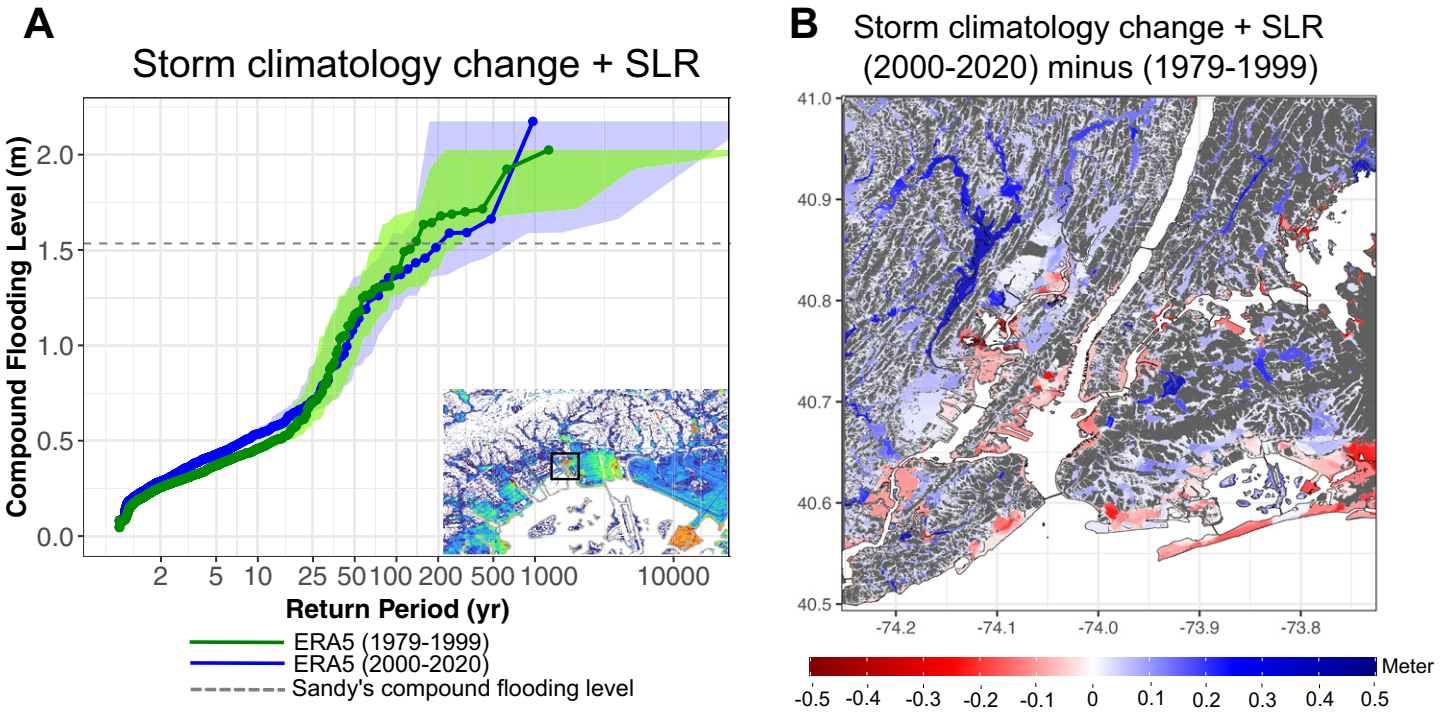


**Fig. 5. Impact of TC climatology change and SLR on the return period of compound flooding in today's climate (2000–20) relative to the end of the twentieth century (1979–99) in NYC. (a) TC compound flooding level as a function of return period, for today's climate and the end of the twentieth century (the results are calculated based on the mean of compound flooding for the depicted area, excluding intertidal ground areas). Each line shows compound flooding results from synthetic TCs generated from ERA5 over each time period. The shading in the figure represents sampling uncertainty bounds calculated based on the 5th and 95th percentiles of a Poisson distribution. The gray dashed line shows the mean of Sandy compound flooding level, calculated from the Sandy-like event (#1299) for the depicted area (shown by a black rectangle). (b) Impact of TC climatology change and SLR on the spatially varying distribution of 100-yr return-period compound flooding events in today's climate relative to the late twentieth century (blue color indicates an upward trend, red color indicates a downward trend, and gray color represents areas with no trend or values close to zero). Water levels are referenced to the vertical datum of NAVD88.**

Figures 6a and 6b show the respective contributions to compound flooding intensification arising from storm climatology changes and SLR. Each curve represents the simulated TC compound flooding events generated from each of the four CMIP6 climate models. Based on the results, the return period of the Sandy-like event (depicted in dash line) is about ~215 years based on the ensemble mean of the four CMIP6 climate models neglecting SLR in the current climate. Going forward in time while still neglecting changes in SLR, the return period of Sandy-like events decreases to ~170 years by the middle of the century, and to ~130 years by the end of the century. With the joint effect of changes in TC climatology and SLR, the Sandy-like event occurs around once in ~150 years in the present climate. The probability of such a damaging event will also increase and become a ~65-yr event by the middle of the century, and a ~30-yr storm by the end of the century. TC climatology changes arising from anthropogenic warming alone will thus increase the probability of a Sandy-like storm by up to 1.26 times by the middle of the century and 1.7 times by the end of the century, relative to the current climate. The joint contribution of TC climatology and SLR will, however, increase the probability of Sandy-like floods by up to almost 2.3 times by the middle of the century, and 5 times by the end of the century. The projected SLR alone will intensify the probability of Sandy's compound flooding by 1.05 times by the middle of the century and 3.3 times by the end of the century relative to the current climate. SLR thus makes a significant contribution to the increased risk of destructive compound flooding events from TCs.

Figures 6c–f show the contribution of each primary driver to the change in 100-yr flooding by the middle and end of the century. The results show that, by the middle of the century,

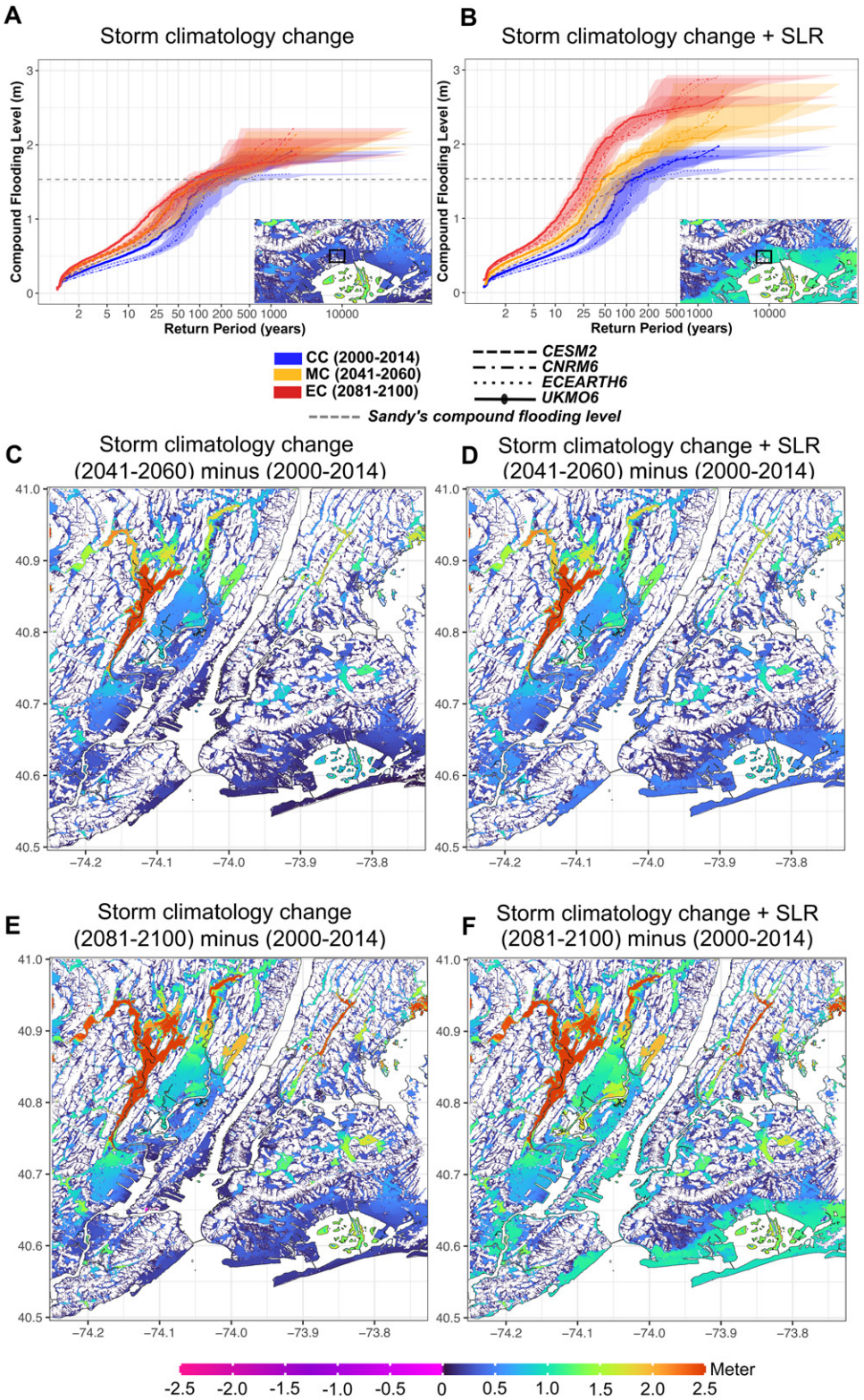


**Fig. 6. Impact of future TC climatology change and SLR on compound flooding in NYC. (a) Contribution of TC climatology change alone, and (b) contribution of both TC climatology change and SLR to the future probability of compound flooding. The results are based on the mean of the compound flooding level (calculated for the depicted coastal area, excluding intertidal ground areas) in the current and future climates. Each line shows the results from synthetic TCs downscaled from each climate model in the current and future climates. The shading in the figure represents confidence intervals calculated based on the 5th and 95th percentiles of a Poisson distribution for each model. The gray dashed line shows the magnitude of compound flooding from Sandy (calculated from the Sandy-like event (#1299) for the depicted area. (c),(d) Impact of TC climatology change and SLR on the spatially varying distribution of 100-yr return-period compound flooding by the middle of the century relative to the current climate, and (e),(f) by the end of the century relative to the current climate. Water levels are referenced to the vertical datum of NAVD88. Note that the spatially varying results are based on the ensemble mean of the four CMIP6 climate models calculated in each climate.**

anthropogenic warming will intensify the level of spatially varying flooding, mostly in inland areas and arising mostly from increased rainfall. A comparison between Fig. 6c and Fig. 6d shows the contribution of SLR to changes in compound flooding by the midcentury. For example, TC climatology change increases the spatially varying compound flooding level, on average, up to ~0.35 m, while the joint contribution of TC changes and SLR will increase flood levels by up to ~0.7 m in coastal areas.

Similarly, TC climatology changes increase rainfall intensity by the end of century, resulting in more increased flooding in inland areas, especially along the Passaic River. This contribution alone increases the level of spatially varying compound flooding by up to almost ~0.5 m by the end of the century in coastal areas (Fig. 6e). The joint impact including SLR, however, increases the level of flooding on average by up to ~1.3 m in the majority of coastal areas by the end of the century (Fig. 6f). These results show the significant impact of SLR in increasing flood risk in NYC. The contributions of both drivers to increasing flood risk for other return periods from 50 to 500 years are given in Figs. S4–S6.

## Compound flooding risk from extratropical cyclones

Figures 7a and 7b show the contributions of ETC climatology changes and SLR to changes in compound flooding over the depicted area. The results cover only high-frequency events (return periods of 20 years or less), due to the temporal limitations of the downscaled dataset, which cannot accommodate low-frequency ETC events exceeding a 20-yr timeframe. With ETC climatology change only, the probability of compound flooding is projected to increase 1.7 times by the middle of the century, and 2.4 times more by the end of the century. The combined impact of ETC climatology change and SLR will, however, increase the probability by a factor of about 5.4 by the middle of the century, and by a factor of about 9 by the end of the century. Considering only SLR, the probability increases by a factor of 3.7 by the middle of the century, and by a factor of 6.6 by the end of the century. In this case, SLR is more important than changes in ETC climatology change in driving increased flooding.

The impacts of ETC storm changes and SLR on the spatially varying distribution of compound flooding for 15-yr return-period events are shown in Figs. 7c and 7d for the middle of the century, and in Figs. 7e and 7f for the end of the century. The results indicate the dominant role of SLR in increasing the incident of ETC-related compound flooding of coastal areas. The results for the impact of ETC climatology changes and SLR on the level of compound flooding for other return periods (5–10 years) are shown in Figs. S7 and S8.

## Discussion

This study introduces a physics-based methodology to comprehensively assess compound flooding risk, surpassing limitations in conventional single-hazard or statistical-based assessments that tend to underestimate flooding risk. In this study we demonstrated the contribution of SLR and TC and ETC climatology changes to intensifying flooding risk in NYC. We found that anthropogenically induced changes to TC activity have already increased flood risk in NYC. This increase translates to more damage from upper tail events, consistent with previous studies on the effect of anthropogenic warming on the incidence and damages of extreme storms (Strauss et al. 2021; Garner et al. 2017; Lin et al. 2016). Our findings reveal that the effect of SLR on flooding from TCs and ETCs has been underestimated, relative to the impact of storm climatology changes in previous studies (Lin et al. 2016, 2012). Most previous studies did not employ spatially detailed hydrodynamic simulations of compound surge- and rainfall-driven flooding. Simpler, often statistical methods used in previous studies are not well suited to quantifying spatially and temporally varying

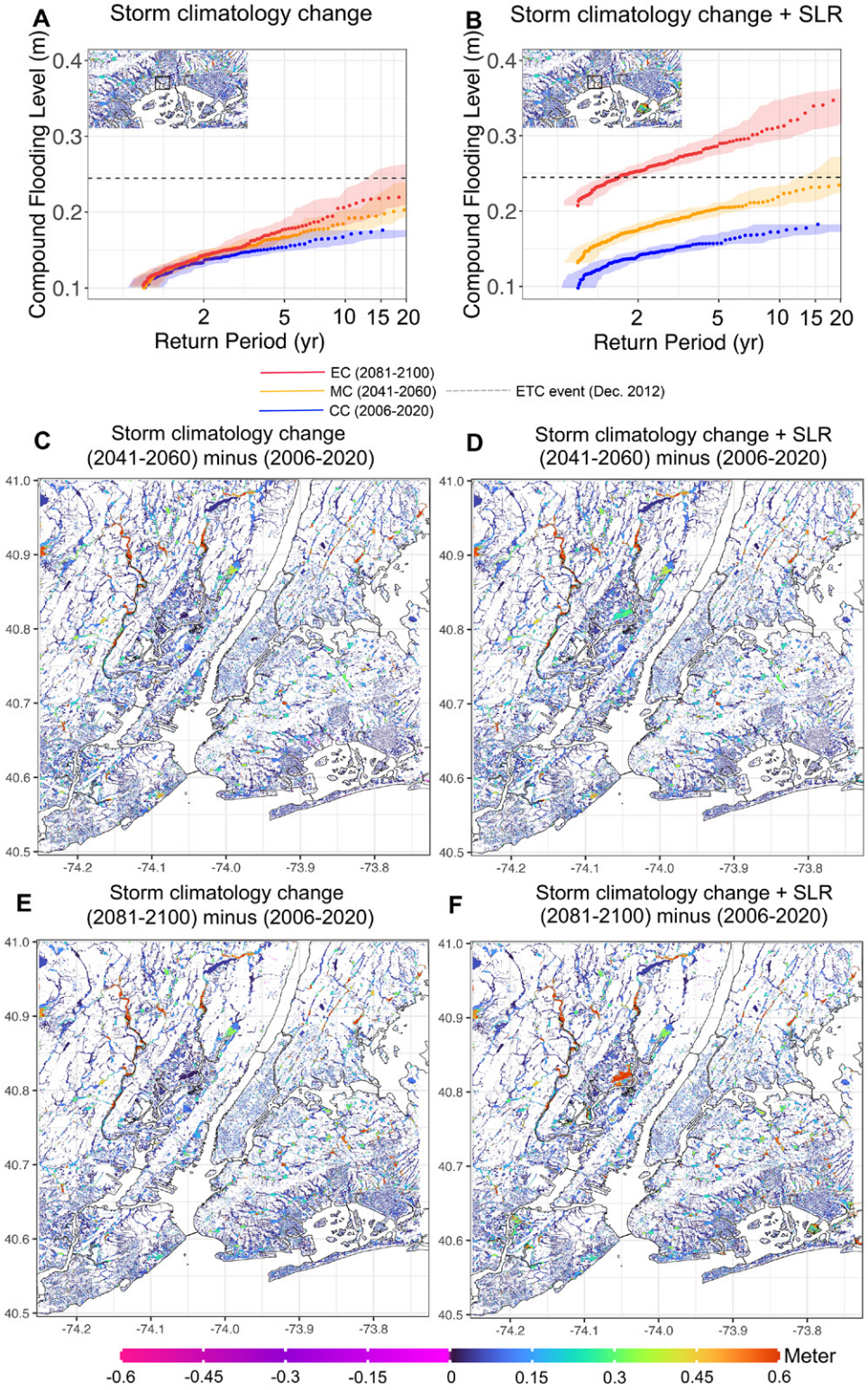


**Fig. 7. Impact of current and future changes in storm climatology and SLR on ETC compound flooding in NYC. (a),(b) Individual and joint contribution of storm climatology changes and SLR on the return period of ETC compound flooding in the current and future climates. The results are based on the mean of compound flooding level calculated for the depicted area, excluding intertidal ground areas. Each line shows the results for ETC events dynamically downscaled by WRF in the current and future climates. The gray dashed line shows the magnitude of compound flooding (m) from the ETC which occurred in December 2012 for the depicted area. (c),(d) Impact of storm climatology changes and SLR on the spatially varying distribution of 15-yr return-period ETC compound flooding events by the middle of the century relative to the current climate, and (e),(f) by the end of the century relative to the current climate (water levels are referenced to the vertical datum of NAVD88).**

flood risk or the contributions of the individual drivers to the net flooding. By ignoring the complex mechanical hydrodynamics of compound flooding, they underestimated the risk of extreme storms such as Hurricane Sandy. According to our numerical physics-based approach, Sandy-like compound flooding occurs around once every ~150 years compared to previous estimates of ~400–500 years (Lin et al. 2016, 2012; Reed et al. 2015), and will occur once every ~65 years by the middle of the century, and once every ~30 years by the end of the century under the SSP3–7.0 scenario. We believe that the current risk of compound flooding from ETCs has also been underestimated in prior studies. We thus provide evidence that the frequency and intensity of compound flooding in NYC from both TCs and ETCs could increase, with rapidly growing risk to communities and infrastructure. Our results are also consistent with the work of Gori et al. (2022), showing that SLR is the most dominant driver of the joint rainfall-surge hazard in the future in NYC.

The approach we use to quantify TC compound flooding hazard is capable of assessing the risk of very low-frequency events, since we can generate an almost unlimited number of synthetic cyclones. By contrast, our assessment of ETC-associated risk is severely circumscribed by the low number of events one can afford to simulate with embedded, three-dimensional models like WRF. Future research should explore better and more efficient ways of downscaling extratropical cyclones. It may be that the only practical way forward is to run ensembles of high-resolution global models in present and future climates and infer ETC climatology directly from the output. This would require extraordinary resources to carry out the simulations and to analyze the resulting output.

While the consideration of astronomical tides and their interaction with surge and relative SLR was not included in our study, we acknowledge their significance and recommend their incorporation in future assessments of surge and compound flood hazard. Despite the omission of tides in our analyses, we observed a strong agreement between historical and simulated surge events (refer to Fig. 3 and Fig. S10). Finally, our TC downscaling is not ideally suited to extratropical transitioning storms like Sandy. As such storms can be very destructive, more work needs to be done on assessing their risk and how they might evolve under climate change.

Overall, this study emphasizes how vulnerable coastal communities are and should serve as a guide to how they might assess and adapt to increasing flooding risk from tropical and extratropical cyclones. Our methodology extends beyond NYC's boundaries, serving as a scalable template for vulnerable coastal regions worldwide facing the threat of compound flooding from TCs and ETCs. However, availability of sufficient data for calibration and evaluation is crucial for accurate assessment and quantification of flood hazard. Customization of the methodology to incorporate region-specific factors such as bathymetry, topsoil characteristics, coastal morphology, storm surge dynamics, and tidal influences is essential. Addressing these challenges would effectively enhance the flexibility and reliability of our methodology, enabling comprehensive assessments of compound flooding in diverse coastal areas.

Our methodology not only quantifies the detailed granular compound flooding risk from TCs and ETCs, accounting for their primary drivers in present and future climatic contexts, but also furnishes decision-makers with scientifically grounded insights to formulate tailored adaptive strategies in coastal urban areas. This empowerment enables authorities to fine-tune adaptation strategies, optimizing resource allocation for enhanced resilience and preparedness in critical infrastructure and vulnerable coastal communities. Such precision is of utmost significance, especially considering the projected 25% increase in population density expected in flood-prone coastal zones and megacities by 2050 (Aerts et al. 2014), alongside SLR and the intensifying storms resulting from anthropogenic warming. In concert

with localized adaptation strategies and the reinforcement of regional resilience, the imperative reduction of greenhouse gas emissions takes on paramount importance in mitigating the heightened risk and minimizing the resulting damages within the context of a warming climate. Our physics-based methodology possesses the capability to assess these scenarios across various climate change projections, enhancing policy-makers' ability to make informed decisions and undertake effective actions.

**Acknowledgments.** The authors thank Muge Komurcu, Matthew Huber, and Stanley Glidden for supplying WRF dynamical downscaling data for ETC events. We acknowledge the World Climate Research Programme, which, through its Working Group on Coupled Modelling, coordinated and promoted CMIP. We thank the climate modeling groups, including CESM1-2, CNRM6, EC-EARTH6, and UKMO6 for producing and making available their model output. This work was financially supported by Homesite Insurance and Plymouth Rock Home. Michael Wiper also acknowledges support from the Spanish Agencia Estatal de Investigación, PID2019-108311GB-100/AEI/10.13039/501100011033.

**Data availability statement.** For surge modeling, historical SLR data at the Battery tide gauge were obtained from NOAA (https://tidesandcurrents.noaa.gov/sltrends/sltrends_station.shtml?id=8518750). The CMIP6 SLR projections under the SSP3–7.0 scenario are also available at https://sealevel.nasa.gov/ipcc-ar6-sea-level-projection-tool?psmsl_id=12. Other information used for flood modeling, including the current bathymetry and coastline features are accessible at www.ncei.noaa.gov/maps/bathymetry/. The lidar-based digital elevation model (DEM) with a computationally feasible spatial resolution of ~20 m to represent the topography of the area is available at https://coast.noaa.gov/dataviewer/. The land-use map to quantify surface roughness is accessible at www.mrlc.gov/. The soil available water storage map to address the rate of topsoil infiltration is also available at https://websoilsurvey.sc.egov.usda.gov/. Other datasets, including TC synthetic tracks and ETC events, are available upon request from the corresponding author, Ali Sarhadi (sarhadi@mit.edu).

## Appendix: Dataset and methodology

***Synthetic TC datasets.*** To address the multiple hazards associated with TCs, a widely used statistical–deterministic downscaling methodology is employed, following the approaches outlined in Emanuel et al. (2006, 2008). This methodology involves random seeding of synthetic TCs across the entire Atlantic Ocean basin, considering spatial location and time of occurrence. Deterministic wind intensity estimation is performed using the high-resolution Coupled Hurricane Intensity Prediction System (CHIPS), a coupled model consisting of an axisymmetric vortex model and a one-dimensional ocean model. The thermodynamic state of the ocean and atmosphere, including monthly mean sea surface temperature, atmospheric temperature, humidity, and daily interpolated horizontal winds at 250 and 850 hPa, drives the randomly initialized vortices in both spatial and temporal dimensions. TCs failing to intensify beyond wind speeds of 21 m $s^{-1}$ (40 kt) are discarded. The method combines the CHIPS model with a theoretical wind model to estimate TC intensity and outer radius, providing insights into cyclone structure and characteristics. There is currently little understanding of the factors that control the overall diameter of TCs. Observations make it clear that the outer radius is lognormally distributed with a mean of around 420 km (Chavas and Emanuel 2010), but we do not have a good idea of how this mean might vary with climate. Variations in the outer radius size are neglected, considering the relatively small size of fluctuations found in previous studies (Schenkel et al. 2023; Chavas and Lin 2016). For the purposes of this study, we fix the outer radius at 400 km, but otherwise the structure of the vortex, including the radius of maximum winds, is determined by the model physics.

We recognize that the overall diameter varies from storm to storm and exerts a strong influence on the extent of wind damage, freshwater flooding, and storm surge, but we do not know enough about the physics to include variations in outer radius here. This dynamic downscaling method enables the simulation of numerous synthetic TC events, driven by climate reanalysis or projections from CMIP6 GCMs, under the assumption that the feedback between TCs and the large-scale environment has minimal impact on their subsequent evolution. The model records maximum surface wind speed, pressure, inner and outer radii of individual synthetic TCs at 2-h intervals throughout their lifetimes. Subsequently, a hydrodynamic model (GeoClaw) uses this information to simulate wind-induced storm surge with high temporal resolution near NYC during TC landfall.

Additionally, we generate rainfall intensity data at an almost 20-m resolution on an hourly basis around the landfall of each synthetic TC in NYC. The accuracy of rainfall estimates from synthetic TC tracks is evaluated in Feldmann et al. (2019) by comparing them to rainfall data obtained from the NEXRAD radar network and rain gauges across the eastern United States. The spatially nonuniformly distributed hourly rainfall intensity data are subsequently employed as input to the hydraulic model, enabling the assessment of the rainfall-induced hazard that contributes to the compound flooding phenomenon in NYC. We acknowledge that despite previous evaluations assessing the performance of the employed rainfall dataset, inherent uncertainties related to spatial nonuniform variability may persist due to various factors, including limitations in input data, modeling assumptions, and parameterizations.

In total, the downscaled datasets, derived from both the reanalysis and climate models, comprise 20,700 synthetic storms, each with their centers passing within a 200-km radius of NYC.

***Extratropical cyclone datasets.*** ETC freshwater flooding events are identified iteratively based on rainfall intensity maxima in a time series, starting from the global maximum and extending four days before to one day after the selected local maximum. The total number of selected events in each downscaled period is 5 times the corresponding number of years. Similarly, surge flooding events are determined by selecting maxima in the coastal-oriented wind component over a 2° × 2° box off the coast of NYC. The extensive selection of rainfall and wind events ensures the inclusion of all significant freshwater and surge flooding possibilities. Compound flood modeling is performed for both wind and rainfall events, excluding TCs by considering events between October and May, acknowledging potential overlap between TCs and ETCs in October.

The WRF simulations employ nested domains on a Cartesian grid, with the innermost 1,500 km × 1,200 km domain using uniform convection-permitting (3-km) resolution. The innermost domain is roughly centered on the state of New York, and encompasses an ocean area that is sufficient to simulate storm surges and rainfall-driven flooding in NYC (Fig. S10). In the context of studying compound flooding in coastal cities, future research efforts may investigate the influence of grid spacing below 3 km on capturing a more precise depiction of extreme precipitation during ETCs. Despite utilizing an optimized spatial resolution in this study, the presence of computational resource limitations may introduce uncertainties in representing the spatial distribution of ETC-related rainfall intensity, stemming from model parameterizations, resolution, and limitations in input data. These uncertainties can have implications for accurately depicting nonuniform precipitation patterns using dynamically downscaled methods. Further research is imperative to enhance the accuracy and resolution of these methods, thereby facilitating an improved representation of nonuniform rainfall distribution.

***Storm surge modeling.*** Storm surge, as defined in previous studies (Reed et al. 2015; Lin et al. 2016; Garner et al. 2017), is an abnormal sea level rise relative to local relative sea level (RSL). It arises from the combined effects of low atmospheric surface pressure and high surface wind speeds associated with ETCs or TCs. The total water level, comprising storm surge and RSL changes, governs the coastal storm surge height. RSL estimation relies on the local mean of total sea level over the climate periods, disregarding interannual variations and the minor nonlinear surge–RSL interaction (Lin et al. 2016).

To simulate storm surge caused by ETCs and synthetic TCs, we employ the GeoClaw numerical model, which utilizes high-resolution shock-capturing finite-volume methods (Mandli and Dawson 2014). Unlike finite-element unstructured hydrodynamic models (Colle et al. 2008; Westerink et al. 2008), GeoClaw incorporates adaptive mesh refinement (AMR) algorithms (Berger et al. 2011; Mandli and Dawson 2014).

The integration of AMR algorithms in the GeoClaw model allows for dynamic mesh refinement in high resolution, enhancing the representation of critical regions and localized surface features. This approach facilitates efficient computational solutions at high resolution and large scale, making it suitable for simulating storm surge from a large ensemble of TCs and ETCs. GeoClaw has effectively simulated storm surge from TCs in diverse coastal regions of the United States, including NYC (Miura et al. 2021; Mandli and Dawson 2014). By implementing essential modifications, we have extended the capabilities of GeoClaw to simulate storm surge induced by ETCs, surpassing the default settings of the out-of-the-box model. To capture surge heights during the landfall of ETCs and TCs near NYC, multiple synthetic gauges were positioned along the coastline, providing high temporal resolution (less than a minute) for the recorded data (Fig. S9). Among these gauges, one is positioned at the Battery gauge site, facilitating a direct comparison between the simulated and observed surge heights.

We evaluated the accuracy of storm surge modeling by comparing simulated surge heights from GeoClaw with observed heights at the Battery gauge during Hurricane Sandy's landfall. After accounting for tidal effects, the surge simulation exhibited high accuracy (Fig. 3). Furthermore, we assessed storm surge modeling for historical ETCs by comparing simulated surge heights from GeoClaw with observed heights for four specific events. Findings on the precision of surge simulation are presented in Fig. S10. These coastal surge simulations can be utilized as boundary conditions in hydraulic models to convert surge heights into surge-driven flooding for compound flooding analysis. We integrate local sea level data into the GeoClaw model, considering values of −0.02 m in the late twentieth century and 0.07 m in the present climate. For future storm surge modeling, we incorporate the ensemble mean of SLR projections from CMIP6, which account for Antarctic and Greenland ice sheets, glaciers, land water storage, vertical land motion, thermal expansion of seawater, and marine ice cliff instability. These projections indicate a total SLR of approximately 0.36 m by the middle of the century (2041–60) and 0.85 m by the end of the century (2081–2100) under the SSP3–7.0 scenario.

***Numerical compound flood modeling.*** To simulate compound surge- and inland heavy rainfall-driven flooding resulting from ETCs and synthetic TCs in NYC, we employ a numerical physically based and computationally efficient 2D hydraulic model. The model used in this study is a modified version of LISFLOOD-FP, a high-resolution hydraulic model that employs an explicit finite-difference scheme to simulate shallow water waves without advection (Neal et al. 2012; Bates et al. 2010). Previous studies have evaluated the performance of this numerical scheme in simulating pluvial, coastal, and fluvial flood modeling (Neal et al. 2012; Wing et al. 2022; Bates et al. 2021). In this study, we improve the LISFLOOD-FP model

by integrating storm surge and rainfall intensity as boundary conditions. This integration allows the model to simulate compound flooding with high spatiotemporal resolution, capturing the complex interaction of storm surge and heavy rainfall during storm landfall.

The model ensures the continuity of mass in each grid cell and the continuity of momentum between cells using the following equations:

$$V_{i,j}^{t+\Delta t} = V_{i,j}^{t} + \Delta t\left(Q_{i-1/2,j}^{t+\Delta t} - Q_{i+1/2,j}^{t+\Delta t} + Q_{i,j-1/2}^{t+\Delta t} - Q_{i,j+1/2}^{t+\Delta t}\right) + \Delta x \Delta y \Delta t\left(P_{i,j}^{t+\Delta t} - I_{i,j}^{t+\Delta t}\right). \quad \text{(A1)}$$

In Eq. (A1), $V_{i,j}^{t}$ and $V_{i,j}^{t+\Delta t}$ represent the volume of compound surge- and rainfall-driven flooding in each cell at time $t$ and $t + \Delta t$, respectively. $Q_{i-(1/2),j}^{t+\Delta t}$ denotes the incoming and outgoing fluxes from surge and rainfall through each cell face, while $\Delta x \Delta y$ represents the surface area of cells. $P_{i,j}^{t+\Delta t}$ corresponds to the incoming rainfall intensity from storms, and $I_{i,j}^{t+\Delta t}$ represents the topsoil infiltration rate in nonconstructed areas. The subscripts $i$ and $j$ refer to the cell spatial indices in the $x$ and $y$ directions, respectively. The model further calculates the compound flooding flow between cells in the area using the continuity of momentum equation:

$$Q_{U,i+1/2}^{t+\Delta t} = \frac{q_{U,i+1/2}^{t} - g h_{U,\text{flow}}^{t} \Delta t S_{i,1/2}^{t}}{1 + g\Delta t n^{2}\left|q_{U,\text{flow}}^{t}\right|\left(h_{U,\text{flow}}^{t}\right)^{7/3}}(\Delta x). \quad \text{(A2)}$$

Here, $Q_{U,i+1/2}^{t+\Delta t}$ represents the compound flood flow between grid cells in the urban area, $q_{U,i+1/2}^{t}$ is the flow from the previous time step, calculated as $Q_{U,i+1/2}^{t}$ divided by the cell width ($\Delta x$), $S_{i,1/2}$ denotes the water surface slope, $n$ is the surface Manning's roughness coefficient, $g$ is the acceleration due to gravity, and $h_{U,\text{flow}}^{t}$ represents the depth of compound flooding flow in the urban area. The model recalculates the flow depth considering $h_{U}^{t}$ and the elevation of each cell. It should be noted that the geodetic datum of NAD83 is utilized to establish the spatial coordinates, while the vertical datum of NAVD88 is used for elevation values within the applied DEM. Additionally, RSL serves as the key factor in distinguishing between land and water elevations. In our study, we utilize a lidar-based DEM with a spatial resolution of approximately 20 m with geographic (latitude–longitude) projection to represent the area's geometry. We also employ a land-use map to quantify surface roughness and a soil available water storage map for the topsoil layer (0–50 cm) to account for the rate of infiltration.

Compound flooding dynamics are simulated at high temporal resolution, capturing maximum flooding levels at each grid cell. Return periods of compound flooding events are calculated using a comprehensive dataset of downscaled TCs and ETCs simulations, enhancing estimation accuracy. We analyze the effects of different factors on compound flooding by conducting two simulations for each storm: one with SLR and one without. This enables quantification of SLR's contribution to spatially varying changes in compound flooding. We also assess the partition of individual components within compound flooding using the same approach. The methodology is summarized in Fig. 1.

## References


Aerts, J. C., W. W. Botzen, K. Emanuel, N. Lin, H. De Moel, and E. O. Michel-Kerjan, 2014: Evaluating flood resilience strategies for coastal megacities. *Science*, **344**, 473–475, https://doi.org/10.1126/science.1248222.

Bakkensen, L. A., and R. O. Mendelsohn, 2019: Global tropical cyclone damages and fatalities under climate change: An updated assessment. *Hurricane Risk*, Springer, 179–197.

Bates, P. D., M. S. Horritt, and T. J. Fewtrell, 2010: A simple inertial formulation of the shallow water equations for efficient two-dimensional flood inundation modelling. *J. Hydrol.*, **387**, 33–45, https://doi.org/10.1016/j.jhydrol.2010.03.027.

——, and Coauthors, 2021: Combined modeling of US fluvial, pluvial, and coastal flood hazard under current and future climates. *Water Resour. Res.*, **57**, e2020WR028673, https://doi.org/10.1029/2020WR028673.

Bender, M. A., T. R. Knutson, R. E. Tuleya, J. J. Sirutis, G. A. Vecchi, S. T. Garner, and I. M. Held, 2010: Modeled impact of anthropogenic warming on the frequency of intense Atlantic hurricanes. *Science*, **327**, 454–458, https://doi.org/10.1126/science.1180568.

Berger, M. J., D. L. George, R. J. LeVeque, and K. T. Mandli, 2011: The GeoClaw software for depth-averaged flows with adaptive refinement. *Adv. Water Resour.*, **34**, 1195–1206, https://doi.org/10.1016/j.advwatres.2011.02.016.

Blake, E. S., T. B. Kimberlain, R. J. Berg, J. P. Cangialosi, and J. L. Beven II, 2013: Tropical cyclone report: Hurricane Sandy (AL182012): 22–29 October 2012. NHC Tech Rep., 157 pp.

Booth, J. F., V. Narinesingh, K. L. Towey, and J. Jeyaratnam, 2021: Storm surge, blocking, and cyclones: A compound hazards analysis for the northeast United States. *J. Appl. Meteor. Climatol.*, **60**, 1531–1544, https://doi.org/10.1175/JAMC-D-21-0062.1.

Chavas, D. R., and K. A. Emanuel, 2010: A QuikSCAT climatology of tropical cyclone size. *Geophys. Res. Lett.*, **37**, L18816, https://doi.org/10.1029/2010GL044558.

——, and N. Lin, 2016: A model for the complete radial structure of the tropical cyclone wind field. Part II: Wind field variability. *J. Atmos. Sci.*, **73**, 3093–3113, https://doi.org/10.1175/JAS-D-15-0185.1.

Colle, B. A., F. Buonaiuto, M. J. Bowman, R. E. Wilson, R. Flood, R. Hunter, A. Mintz, and D. Hill, 2008: New York City's vulnerability to coastal flooding: Storm surge modeling of past cyclones. *Bull. Amer. Meteor. Soc.*, **89**, 829–842, https://doi.org/10.1175/2007BAMS2401.1.

Emanuel, K., 2005: Increasing destructiveness of tropical cyclones over the past 30 years. *Nature*, **436**, 686–688, https://doi.org/10.1038/nature03906.

——, 2013: Downscaling CMIP5 climate models shows increased tropical cyclone activity over the 21st century. *Proc. Natl. Acad. Sci. USA*, **110**, 12 219–12 224, https://doi.org/10.1073/pnas.1301293110.

——, 2017: Assessing the present and future probability of Hurricane Harvey's rainfall. *Proc. Natl. Acad. Sci. USA*, **114**, 12 681–12 684, https://doi.org/10.1073/pnas.1716222114.

——, 2021a: Atlantic tropical cyclones downscaled from climate reanalyses show increasing activity over past 150 years. *Nat. Commun.*, **12**, 7027, https://doi.org/10.1038/s41467-021-27364-8.

——, 2021b: Response of global tropical cyclone activity to increasing $CO_2$: Results from downscaling CMIP6 models. *J. Climate*, **34**, 57–70, https://doi.org/10.1175/JCLI-D-20-0367.1.

——, S. Ravela, E. Vivant, and C. Risi, 2006: A statistical deterministic approach to hurricane risk assessment. *Bull. Amer. Meteor. Soc.*, **87**, 299–314, https://doi.org/10.1175/BAMS-87-3-299.

——, R. Sundararajan, and J. Williams, 2008: Hurricanes and global warming: Results from downscaling IPCC AR4 simulations. *Bull. Amer. Meteor. Soc.*, **89**, 347–368, https://doi.org/10.1175/BAMS-89-3-347.

Feldmann, M., K. Emanuel, L. Zhu, and U. Lohmann, 2019: Estimation of Atlantic tropical cyclone rainfall frequency in the United States. *J. Appl. Meteor. Climatol.*, **58**, 1853–1866, https://doi.org/10.1175/JAMC-D-19-0011.1.

Garner, A. J., and Coauthors, 2017: Impact of climate change on New York City's coastal flood hazard: Increasing flood heights from the preindustrial to 2300 CE. *Proc. Natl. Acad. Sci. USA*, **114**, 11 861–11 866, https://doi.org/10.1073/pnas.1703568114.

Gori, A., and N. Lin, 2022: Projecting compound flood hazard under climate change with physical models and joint probability methods. *Earth's Future*, **10**, e2022EF003097, https://doi.org/10.1029/2022EF003097.

——, ——, D. Xi, and K. Emanuel, 2022: Tropical cyclone climatology change greatly exacerbates US extreme rainfall–surge hazard. *Nat. Climate Change*, **12**, 171–178, https://doi.org/10.1038/s41558-021-01272-7.

Huang, P., I.-I. Lin, C. Chou, and R.-H. Huang, 2015: Change in ocean subsurface environment to suppress tropical cyclone intensification under global warming. *Nat. Commun.*, **6**, 7188, https://doi.org/10.1038/ncomms8188.

Komurcu, M., K. Emanuel, M. Huber, and R. Acosta, 2018: High-resolution climate projections for the northeastern United States using dynamical downscaling at convection-permitting scales. *Earth Space Sci.*, **5**, 801–826, https://doi.org/10.1029/2018EA000426.

Kossin, J. P., K. A. Emanuel, and G. A. Vecchi, 2014: The poleward migration of the location of tropical cyclone maximum intensity. *Nature*, **509**, 349–352, https://doi.org/10.1038/nature13278.

Levinson, M. J., 2018: Impacts of drainage basin characteristics on aquatic macroinvertebrate communities in the upper Passaic River. M.S. thesis, Dept. of Biology, Montclair State University, 147 pp., https://digitalcommons.montclair.edu/etd/106/.

Lin, N., K. Emanuel, M. Oppenheimer, and E. Vanmarcke, 2012: Physically based assessment of hurricane surge threat under climate change. *Nat. Climate Change*, **2**, 462–467, https://doi.org/10.1038/nclimate1389.

——, R. E. Kopp, B. P. Horton, and J. P. Donnelly, 2016: Hurricane Sandy's flood frequency increasing from year 1800 to 2100. *Proc. Natl. Acad. Sci. USA*, **113**, 12 071–12 075, https://doi.org/10.1073/pnas.1604386113.

——, R. Marsooli, and B. A. Colle, 2019: Storm surge return levels induced by mid-to-late-twenty-first-century extratropical cyclones in the northeastern United States. *Climatic Change*, **154**, 143–158, https://doi.org/10.1007/s10584-019-02431-8.

Mandli, K. T., and C. N. Dawson, 2014: Adaptive mesh refinement for storm surge. *Ocean Modell.*, **75**, 36–50, https://doi.org/10.1016/j.ocemod.2014.01.002.

Marsooli, R., N. Lin, K. Emanuel, and K. Feng, 2019: Climate change exacerbates hurricane flood hazards along US Atlantic and Gulf coasts in spatially varying patterns. *Nat. Commun.*, **10**, 3785, https://doi.org/10.1038/s41467-019-11755-z.

Miura, Y., K. T. Mandli, and G. Deodatis, 2021: High-speed GIS-based simulation of storm surge–induced flooding accounting for sea level rise. *Nat. Hazards Rev.*, **22**, 04021018, https://doi.org/10.1061/(ASCE)NH.1527-6996.0000465.

Moftakhari, H. R., G. Salvadori, A. AghaKouchak, B. F. Sanders, and R. A. Matthew, 2017: Compounding effects of sea level rise and fluvial flooding. *Proc. Natl. Acad. Sci. USA*, **114**, 9785–9790, https://doi.org/10.1073/pnas.1620325114.

Neal, J., G. Schumann, and P. Bates, 2012: A subgrid channel model for simulating river hydraulics and floodplain inundation over large and data sparse areas. *Water Resour. Res.*, **48**, W11506, https://doi.org/10.1029/2012WR012514.

Palm, R., and T. Bolsen, 2023: Perspectives of southwest Florida homeowners and real estate agents before Hurricane Ian. *Prof. Geogr.*, **75**, 916–931, https://doi.org/10.1080/00330124.2023.2194372.

Patricola, C. M., and M. F. Wehner, 2018: Anthropogenic influences on major tropical cyclone events. *Nature*, **563**, 339–346, https://doi.org/10.1038/s41586-018-0673-2.

Priestley, M. D., and J. L. Catto, 2022: Future changes in the extratropical storm tracks and cyclone intensity, wind speed, and structure. *Wea. Climate Dyn.*, **3**, 337–360, https://doi.org/10.5194/wcd-3-337-2022.

Rappaport, E. N., 2014: Fatalities in the United States from Atlantic tropical cyclones: New data and interpretation. *Bull. Amer. Meteor. Soc.*, **95**, 341–346, https://doi.org/10.1175/BAMS-D-12-00074.1.

Reed, A. J., M. E. Mann, K. A. Emanuel, N. Lin, B. P. Horton, A. C. Kemp, and J. P. Donnelly, 2015: Increased threat of tropical cyclones and coastal flooding to New York City during the anthropogenic era. *Proc. Natl. Acad. Sci. USA*, **112**, 12 610–12 615, https://doi.org/10.1073/pnas.1513127112.

Roberts, K. J., B. A. Colle, and N. Korfe, 2017: Impact of simulated twenty-first-century changes in extratropical cyclones on coastal flooding at the battery, New York City. *J. Appl. Meteor. Climatol.*, **56**, 415–432, https://doi.org/10.1175/JAMC-D-16-0088.1.

Saleh, F., V. Ramaswamy, Y. Wang, N. Georgas, A. Blumberg, and J. Pullen, 2017: A multi-scale ensemble-based framework for forecasting compound coastal-riverine flooding: The Hackensack-Passaic watershed and Newark Bay. *Adv. Water Resour.*, **110**, 371–386, https://doi.org/10.1016/j.advwatres.2017.10.026.

Saunders, M. A., and A. S. Lea, 2008: Large contribution of sea surface warming to recent increase in Atlantic hurricane activity. *Nature*, **451**, 557–560, https://doi.org/10.1038/nature06422.

Schenkel, B. A., D. Chavas, N. Lin, T. Knutson, G. Vecchi, and A. Brammer, 2023: North Atlantic tropical cyclone outer size and structure remain unchanged by the late twenty-first century. *J. Climate*, **36**, 359–382, https://doi.org/10.1175/JCLI-D-22-0066.1.

Smith, A. B., 2020: US billion-dollar weather and climate disasters, 1980–present (NCEI Accession 0209268). NOAA NCEI, accessed 17 April 2023, https://doi.org/10.25921/stkw-7w73.

Strauss, B. H., and Coauthors, 2021: Economic damages from hurricane sandy attributable to sea level rise caused by anthropogenic climate change. *Nat. Commun.*, **12**, 2720, https://doi.org/10.1038/s41467-021-22838-1.

Trenberth, K. E., L. Cheng, P. Jacobs, Y. Zhang, and J. Fasullo, 2018: Hurricane Harvey links to ocean heat content and climate change adaptation. *Earth's Future*, **6**, 730–744, https://doi.org/10.1029/2018EF000825.

Wahl, T., S. Jain, J. Bender, S. D. Meyers, and M. E. Luther, 2015: Increasing risk of compound flooding from storm surge and rainfall for major US cities. *Nat. Climate Change*, **5**, 1093–1097, https://doi.org/10.1038/nclimate2736.

Walsh, K. J., and Coauthors, 2015: Hurricanes and climate: The U.S. CLIVAR working group on hurricanes. *Bull. Amer. Meteor. Soc.*, **96**, 997–1017, https://doi.org/10.1175/BAMS-D-13-00242.1.

Waters, M. C., 2016: Life after Hurricane Katrina: The Resilience In Survivors of Katrina (RISK) project. *Sociol. Forum*, **31**, 750–769, https://doi.org/10.1111/socf.12271.

Westerink, J. J., and Coauthors, 2008: A basin- to channel-scale unstructured grid hurricane storm surge model applied to southern Louisiana. *Mon. Wea. Rev.*, **136**, 833–864, https://doi.org/10.1175/2007MWR1946.1.

Wing, O. E., and Coauthors, 2022: Inequitable patterns of US flood risk in the Anthropocene. *Nat. Climate Change*, **12**, 156–162, https://doi.org/10.1038/s41558-021-01265-6.

Xi, D., and N. Lin, 2022a: Investigating the physical drivers for the increasing tropical cyclone rainfall hazard in the United States. *Geophys. Res. Lett.*, **49**, e2022GL099196, https://doi.org/10.1029/2022GL099196.

——, and ——, 2022b: Understanding uncertainties in tropical cyclone rainfall hazard modeling using synthetic storms. *J. Hydrometeor.*, **23**, 925–946, https://doi.org/10.1175/JHM-D-21-0208.1.

Zhang, W., G. Villarini, G. A. Vecchi, and J. A. Smith, 2018: Urbanization exacerbated the rainfall and flooding caused by Hurricane Harvey in Houston. *Nature*, **563**, 384–388, https://doi.org/10.1038/s41586-018-0676-z.